Transmission Electron Microscopy Examination of Hardening and Toughening Phenomena in Aermet 100

RAGHAVAN AYER and P.M. MACHMEIER

The effect of tempering on the microstructure and mechanical properties of ultrahigh strength Aermet 100 steel was examined. In the as-quenched condition, the steel contained a dispersion of relatively fine, undissolved, (CrTiFeMo)C and $(CrFeMo)_{23}C_6$ carbides in a martensitic matrix. Upon tempering at 427 °C, the martensite decomposed to form a high density of cementite particles concomitant with a significant drop in toughness. Tempering at 454 °C resulted in peak strength (yield strength ~ 1756 MPa) due to the precipitation of coherent zones of fine carbides. The peak in toughness (170 $MPa\sqrt{m}$), attained at a tempering temperature of 482 °C, was attributed to both the absence of cementite and the formation of reverted, stable austenite. Tempering at higher temperatures resulted in loss of both strength and toughness, which was suggested to be the result of precipitate coarsening and formation of unstable austenite, respectively. The details of the electron microscopy studies and mechanism of strengthening and toughening are discussed in light of the current understanding of this subject.

I. INTRODUCTION

HIGH performance applications require materials with ultrahigh strength capability with good fracture toughness and fatigue resistance. Therefore, over the past several decades, there has been extensive interest in the structure and mechanical properties of secondary hardening ultrahigh strength steels. The initial studies during the sixties and seventies focused on the microstructure and mechanical properties of simple Fe-M-C systems where M would consist of one or more elements (such as Mo, W, V, Cr, *etc.*) which are known to cause secondary hardening.[1–13] Other investigations disclosed that cobalt additions to Fe-Ni-Mo-C steels resulted in an increase in (1) the M_s temperature, (2) the activity coefficient of carbon resulting in enhanced diffusion, and (3) solid solution strengthening.[14–17] The microstructure of steels containing cobalt was shown to exhibit a higher rate of M_2C carbide nucleation, increased particle refinement, and a decreased propensity to austenite reversion upon tempering. The precipitation of the fine M_2C-type carbides was attributed to the delayed recovery of the dislocation substructure of the martensite in Fe-Mo-C steels containing cobalt.[14,16,17] The subsequent work by Speich established the basis for the new generation of alloy steels containing nickel and cobalt where the combination of high strength and toughness was emphasized.[16,17] These concepts led to the development of AF 1410 steel and other ultrahigh strength steels with superior toughness by Machmeier and co-workers.[18,19] The mechanisms of strengthening, with particular emphasis on carbide composition, crystal structure, and coarsening in these steels, were extensively studied by Olson and other workers.[20–30]

Based on improved melting techniques and some alloy modifications, Schmidt and Hemphill recently developed a new high performance steel, Aermet 100, which exhibited even higher strength and toughness compared to AF 1410.[31,32] However, a fundamental understanding of the critical microstructural features which provided the high strength and toughness in this steel is still not clear. Therefore, the present study was undertaken to conduct a detailed microstructural analysis of Aermet 100 steel to understand the variations in strength and toughness during tempering. Transmission electron microscopy (TEM) and X-ray diffraction were used to characterize the strengthening carbides and austenite, and X-ray line broadening analysis was performed to determine the onset of recovery in the martensite. An overview of the study was reported in a recent symposium,[33] and the details of the experimental results are described in this article.

II. EXPERIMENTAL PROCEDURE

The composition of the steel investigated in this study is listed in Table I. The steel was VIM/VAR melted and forged/rolled to 67 and 21 mm rounds, respectively. Blanks of the steel were austenitized at 843 °C for 1 hour, quenched in oil to room temperature, and immediately transferred to a cryogenic bath held at −73.3 °C. One piece was saved and the other pieces were tempered at 427 °C, 454 °C, 468 °C, 482 °C, 510 °C, 538 °C, 566 °C, or 593 °C for 5 hours. Tensile, single edge bend (SEB), and compact tension (CT) specimens were machined from the heat-treated blanks in the L-T orientation. Finish machining resulted in 6.4-mm-diameter tensile, 10 × 10 × 55 mm SEB, and 25.4-mm-thick CT specimens. Tensile tests were conducted at room temperature per ASTM E8-91 at a strain rate of $10^{-4}s^{-1}$ using an MTS 810 Universal Testing Machine and Masscomp Data Acquisition System.

Estimated mode I fracture toughness, K_Q, was measured by precracked (a/W = 0.45 to 0.55) three-point SEB specimens and standard CT specimens using linear elastic fracture mechanics (LEFM) criteria per ASTM 399-90. The testing of several SEB and CT specimens at the highest strength levels provided valid plane strain

RAGHAVEN AYER is with STEM, Inc., Woodbridge, CT 06525. P.M. MACHMEIER, Manager–Materials and Process Engineering, is with Snap-on Tools Corp., Kenosha, WI 53141.

Manuscript submitted January 6, 1993.

Table I. Composition of Steel (Weight Percent)

C	0.23	Si	0.01
Co	13.4	Al	0.004
Ni	11.08	Ti	0.013
Cr	3.04	S	0.001
Mo	1.2	P	0.003
Mn	0.02	Fe	balance

fracture toughness values, K_{Ic}, as described in Section III–A.

Thin specimens for TEM were cut from the heat-treated blanks, ground to about 75 μm, and electropolished in a perchloric acid-methanol solution at −40 °C. Only samples tempered at 427 °C, 454 °C, 482 °C, 510 °C, 538 °C, and 566 °C were examined in the TEM. The second-phase particles present in the samples were too small to be analyzed in thin specimens without matrix interference. Therefore, the chemical composition and crystal structures of these particles were determined by TEM after extracting them in carbon replicas. The replicas were prepared by evaporating a thin film of carbon on polished and etched specimens. The film was floated in the electropolishing electrolyte and supported on a copper grid. Spectra from individual precipitates were collected and analyzed by thin film analysis using independent k values. Electron diffraction was performed with a convergent, 12-nm-diameter probe and a 20-μm C_2 aperture.

The volume fraction of retained and/or reverted austenite* was determined by X-ray diffraction using the method outlined by Miller.[34] Root-mean-square (RMS) strain along the $[110]_\alpha$ (α refers to the martensite matrix) direction was determined from the line broadening of the martensite peaks. The methodology was originally described by Warren[35] and Warren and Averbach[36] and recently adopted by Ganesan *et al.*[37] The profiles of (110) and (220) peaks of martensite for the tempered samples and the standard were recorded using a CuK_α radiation, with an armco iron sample slow cooled from 950 °C being used as the standard. The RMS strain at 5 nm column length was obtained by Fourier analysis, as outlined by Ganesan *et al.*[37]

*The term *retained austenite* is used to refer to austenite present in the as-quenched condition. The term *reverted austenite* is used to refer to austenite which formed during subsequent tempering, above A_1.

III. RESULTS

A. *Mechanical Properties*

The effect of tempering of the secondary hardening steel over a range of temperatures resulted in substantial changes in tensile and yield strengths and estimated fracture toughness, K_Q, values, as shown in Figure 1. Valid plane strain fracture toughness measurements, K_{Ic}, were only obtained at two tempering temperatures, and these values are indicated by asterisk on the plot. Deviations of the estimated values from the valid plane strain values were determined on samples that were heat-treated to achieve peak hardening. At the tempering temperature

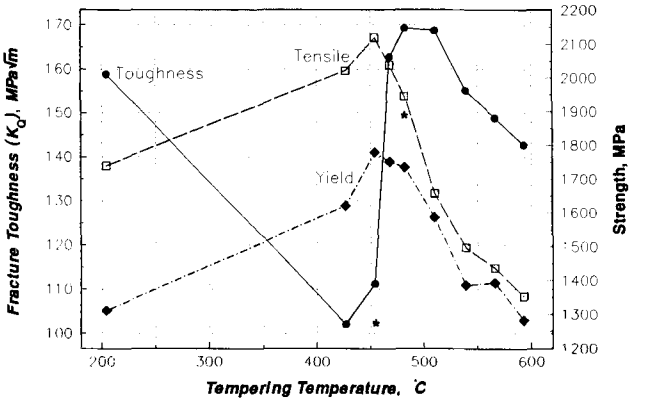

Fig. 1 — Variation of yield and tensile strengths and estimated plane strain fracture toughness (K_Q) with tempering temperature. The fracture toughness values indicated by an asterisk are valid plane strain fracture toughness values (K_{Ic}).

of 454 °C, one of the fracture toughness tests yielded a valid K_{IC} of 102.4 MPa$\sqrt{m}$ while a duplicate test yielded a K_Q value of 119.7 MPa$\sqrt{m}$. Similarly, at 482 °C, an SEB specimen yielded a K_Q value of 169.4 MPa$\sqrt{m}$ compared to a valid K_{Ic} value of 149.3 MPa$\sqrt{m}$ for a CT specimen. Comparison of these K_Q and K_{Ic} values indicated that the K_Q values are within 13 to 16 pct of valid K_{Ic} values in the peak hardening range.

The yield and tensile strengths of the steel increased upon tempering and then peaked when tempered at 454 °C. When the steel was tempered above 454 °C, the tensile strength decreased rapidly while the yield strength decreased slowly until 482 °C above which it decreased rapidly. The fracture toughness of the steel showed a minimum when tempered at 427 °C followed by a small increase when tempered at 454 °C. Tempering at 468 °C resulted in a substantial increase (~50 pct) in the toughness, and the maximum toughness values were obtained when the steel was tempered at 482 °C or 510 °C. Tempering above 510 °C resulted in a rapid drop in the fracture toughness. The optimum combination of tensile strength and fracture toughness was obtained at the tempering temperature of 468 °C.

B. *TEM Analysis*

1. *As-quenched*

The quenched and cryogenically treated steel was completely martensitic with little retained austenite. (When the steel was not cryogenically treated, it would contain about 1.8 vol pct retained austenite.) The microstructure predominantly consisted of a mixture of twinned (30 pct) and untwinned plates (Figure 2). Auto-

*The term *plate* rather than *lath* is used in the present context, since the individual units were separated by high-angle boundaries. The nature of the boundaries was qualitatively determined by obtaining diffraction patterns from contiguous units.

tempering was not observed, ostensibly due to the low M_s temperature of the steel. The steel contained a fine dispersion of spherical particles which were analyzed in the extraction replica (Figure 3(a)). Two types of particles were observed. One set of particles, which ranged

Fig. 2—Bright-field images of as-quenched and cryogenically treated steel showing martensite plates and twins.

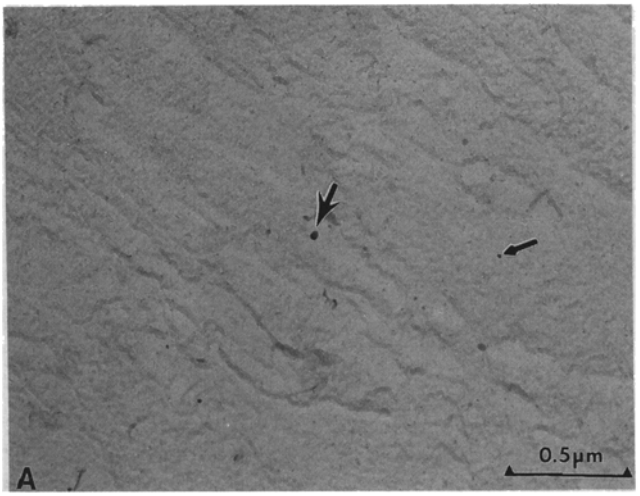

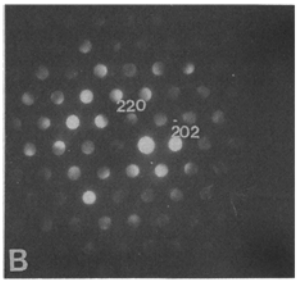

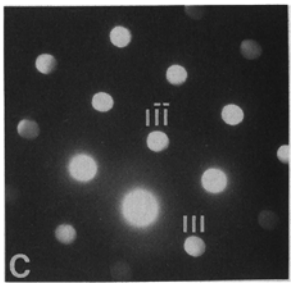

Fig. 3—(*a*) Bright-field image of an extraction replica of the as-quenched and cryogenically treated steel showing fine MC-type carbides (small arrow) and relatively coarser $M_{23}C_6$ carbides (large arrow); electron diffraction patterns from these particles are shown in (*b*) $[1\bar{1}1]_{MC}$ and (*c*) $[01\bar{1}]_{M23C6}$.

in size from 5 to 12 nm, was identified to be a cubic MC carbide with a stoichiometry of $(Cr_{0.3}Ti_{0.3}Mo_{0.3}Fe_{0.1})C$ (Figure 3(b)). The other set of particles was coarser, about 20 to 100 nm in size, and was identified to be $(Cr_{0.58}Fe_{0.36}Mo_{0.06})_{23}C_6$ by electron diffraction (Figure 3(c)). Isolated instances of faulted carbides were also observed, these carbides were identified by electron diffraction to be Cr_7C_3.

2. *Tempering at 427 °C*

Tempering resulted in the formation of relatively coarse Widmanstätten cementite on the {110} planes of martensite and elongated cementite at the plate and twin boundaries, as shown in Figures 4(a) and (b). The martensitic substructure did not show any microstructural features indicating recovery.

3. *Tempering at 454 °C*

Cementite particles that were present within the plates upon tempering at 427 °C were absent after tempering at 454 °C. Cementite was present as isolated precipitates at the prior austenite grain boundaries (Figures 5(a) and (b)). The precipitation at the grain boundaries was not extensive, and many boundaries did not contain any particles.

In the martensitic matrix, extremely fine, needle-shaped precipitates were observed. Since the long dimension of the needles is parallel to the ⟨100⟩ direction of the matrix,[9,10,11] images of the needle-shaped precipitates were obtained at a foil orientation of $[001]_\alpha$. These images enabled the determination of the length and diameter of the precipitates. Figure 6(a) is a bright-field image obtained at close to [001] matrix orientation, showing strain contrast resulting from coherency strains. In addition to the elongated precipitates, small dots are also seen in the image (indicated by arrows) corresponding to the "end-on" view of the needles.

Electron diffraction analysis was attempted to identify the crystal structure of the needle precipitates. Figure 7(a) shows a $[001]_\alpha$ diffraction pattern obtained from a martensite plate using a 20-μm C_2 aperture. The pattern showed diffuse intensities, but discernable intensity maxima attributable to precipitates were not observed. Based on the electron diffraction evidence, it was not possible to determine the characteristics of the fine precipitates.

Attempts to extract the precipitates by carbon replication were not successful, as seen in the bright-field image and electron diffraction pattern (Figure 8). The bright-field image only showed the spherical carbides which were present in the as-quenched condition, and the electron diffraction pattern did not show any reflections that could be associated with the M_2C carbide or any other crystalline phase.

4. *Tempered at 482 °C*

The sample tempered at 482 °C revealed that the grain boundary cementite particles were absent and the needle-shaped precipitates in the matrix had grown in size. Figure 6(b) is a typical bright-field image obtained close to a $[001]_\alpha$ orientation, showing the needle-shaped precipitates; many of the precipitates exhibited strain contrast, indicating they still maintained coherency with the matrix. Some of the precipitates, however, did not show any discernable strain contrast, and it was concluded that

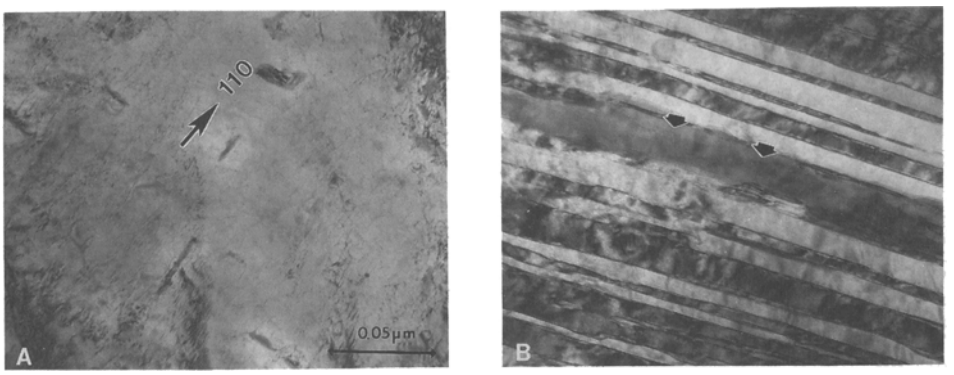

Fig. 4—Sample tempered at 427 °C; bright-field images showing the formation of cementite: (*a*) intraplate Widmanstätten platelets and (*b*) along twin boundaries (arrows).

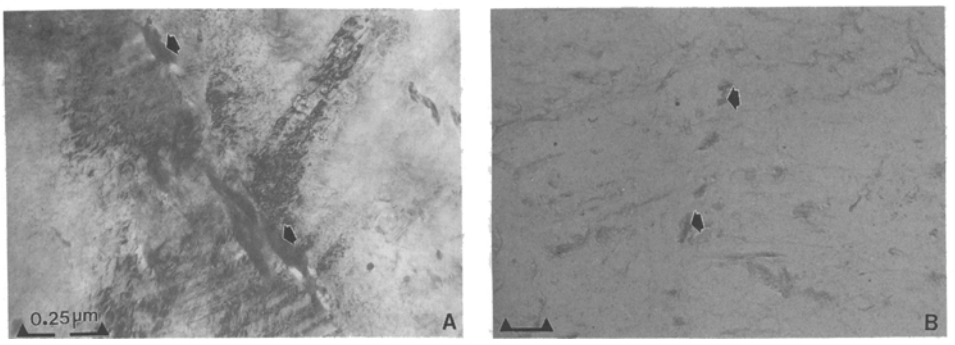

Fig. 5—Sample tempered at 454 °C: (*a*) thin-foil and (*b*) extraction replica bright-field images showing cementite precipitation at prior austenite grain boundaries (arrows).

at least some of the precipitates had lost coherency. As observed in the sample tempered at 454 °C, the end-on precipitates were seen as dots in the image.

Selected area electron diffraction of martensite plates at a $[001]_\alpha$ orientation was examined for precipitate reflections (Figure 7(b)). The pattern showed streaking along the $[100]_\alpha$ and [010] directions of the martensitic matrix from the needles lying along the $[010]_\alpha$ and $[100]_\alpha$ directions, respectively. In order to analyze the crystal structure of the precipitates, attempts were made to obtain diffraction patterns from individual needles with a 12-nm probe; however, no diffraction spots were observed.

Extraction replicas obtained from the sample were examined to determine the structure and chemistry of the precipitates, and a typical bright-field image is shown in Figure 9(a). The selected area diffraction pattern obtained from the replica is shown in Figure 9(b). The pattern showed one faint ring (arrow, Figure 9(b)) which was identified to arise from the $\{1\bar{1}1\}$ planes of the hexagonal M_2C carbide. Electron diffraction was attempted on several individual precipitates to examine if all the precipitates had the hexagonal structure. Diffraction spots were not observed from most precipitates, but some of them showed patterns that could be indexed as the M_2C carbide, an example is shown in Figure 9(c). It was concluded that at least some of the precipitates present in the sample were crystalline M_2C carbides with the well-known hexagonal structure.[11]

The bright-field images showed the formation of austenite at the plate boundaries in a thin-film morphology (Figures 10(a) and (b)). The formation of austenite was clearly evident in the defocussed bright-field images (Figure 10(b)) and subsequently confirmed by dark-field imaging (Figure 10(c)). The thickness of the austenite film was small, about 3 nm, and it was not possible to determine if it formed by nucleation and growth or by reverse shear.[39]

5. *Tempered at 510 °C*

Besides precipitate coarsening, tempering at 510 °C resulted in (1) loss of precipitate/matrix coherency and (2) increased volume fraction of reverted austenite. Figure 6(c) shows a bright-field image obtained close to the $[001]_\alpha$ orientation, and the three variants of the needles are clearly seen in the image. The loss of coherency is evidenced by the absence of the strain contrast and the presence of fringes. Appreciable reversion of austenite was observed along the plate boundaries (Figure 11(a)). Examination showed the reverted austenite formed primarily at the plate boundaries with a Kurdjumov-Sachs relationship (Figures 11(b) and (c)). The austenite was free of any dislocations, indicating that they had formed by nucleation and growth.

Electron diffraction analysis was conducted in thin foils to determine the crystallographic relationship of the carbides with the matrix. Figures 12(a) and (b) are diffraction patterns of the $[001]_\alpha$ orientation of the matrix, showing reflections from the two M_2C precipitate variants in the plane of the foil. The schematic indexing of the pattern is shown in Figure 12(b); the pattern shows reflections expected from all three variants, but only

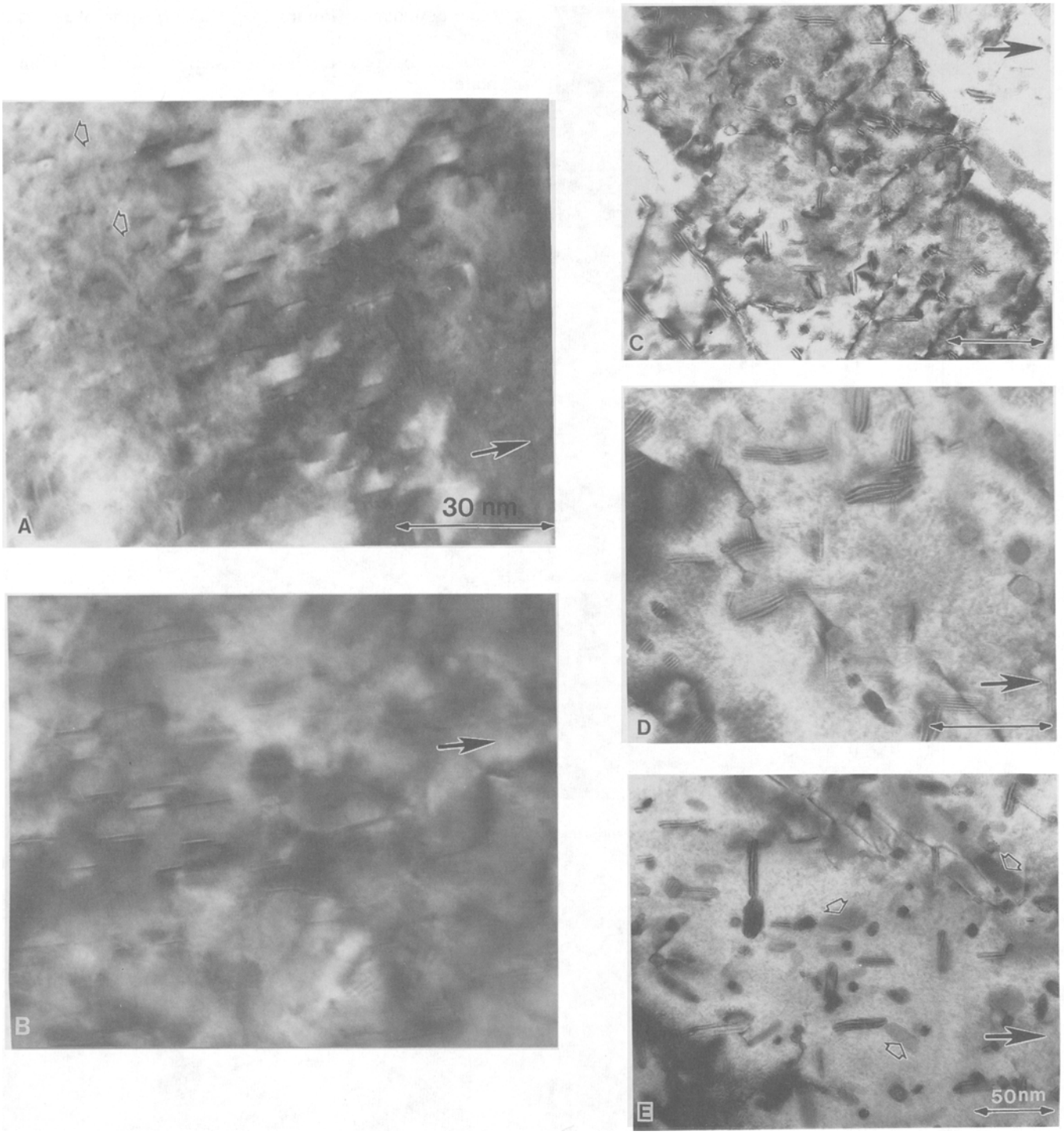

Fig. 6—Bright-field images obtained at [100] orientation of samples tempered at (*a*) 454 °C, (*b*) 482 °C, (*c*) 510 °C, (*d*) 538 °C, and (*e*) 566 °C. Long arrows indicate the [010] direction. Broad arrows indicate the end-on precipitates in (*a*) and austenite particles in (*e*).

flections from the two variants in the plane of the foil are seen in Figure 12(a).

A bright-field image of the carbon extraction replica and a selected area electron diffraction pattern are shown in Figures 13(a) and (b). The bright-field image (Figure 13(a)) showed elongated precipitates, and a ring pattern from the precipitates (Figure 13(b)) can be unambiguously indexed to arise from the hexagonal M_2C carbides.

6. *Tempered at 538 °C or 566 °C*

Tempering at 538 °C or 566 °C resulted in coarsening of the precipitates (Figures 6(d) and (e)). As expected, increased austenite reversion was observed at these temperatures and austenite formed predominantly at the

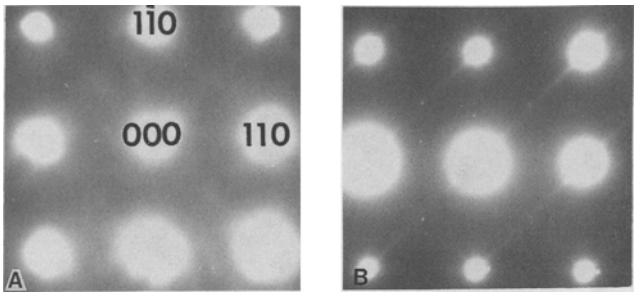

Fig. 7—[001] electron diffraction patterns from martensite; sample tempered at (*a*) 454 °C showing diffuse intensity and (*b*) 482 °C showing streaking along [100] and [010] directions.

plate boundaries (Figure 14). The formation of reverted intra-plate austenite was evident after tempering at 566 °C; figure 6(e) shows austenite particles within a plate.

7. *Size and Composition of M_2C Carbide*

The length and diameter of the carbides were measured from the [001] bright-field images in the TEM (Figure 15). Extraction replicas were not used, because it was necessary to orient the needles along and normal to the needle axis for proper determination of length and diameter. The size of the precipitates at 454 °C and 482 °C tempering indicated in the plot could be overestimated due to the presence of strain fields; size determinations at higher tempering temperatures are considered more accurate. The plot shows that the rate of change in precipitate length with tempering temperature was low below 482 °C; above this temperature, the

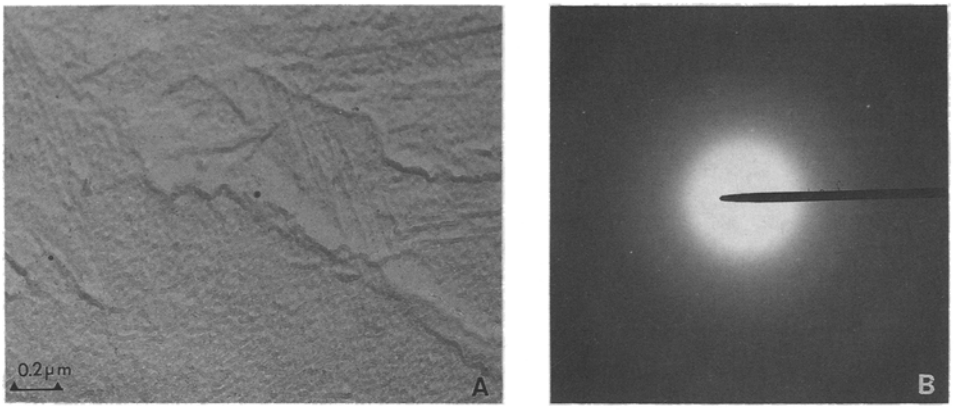

Fig. 8—Sample tempered at 454 °C: (*a*) bright-field image and (*b*) selected area diffraction pattern from extraction replica, showing no diffraction intensities from strengthening precipitates.

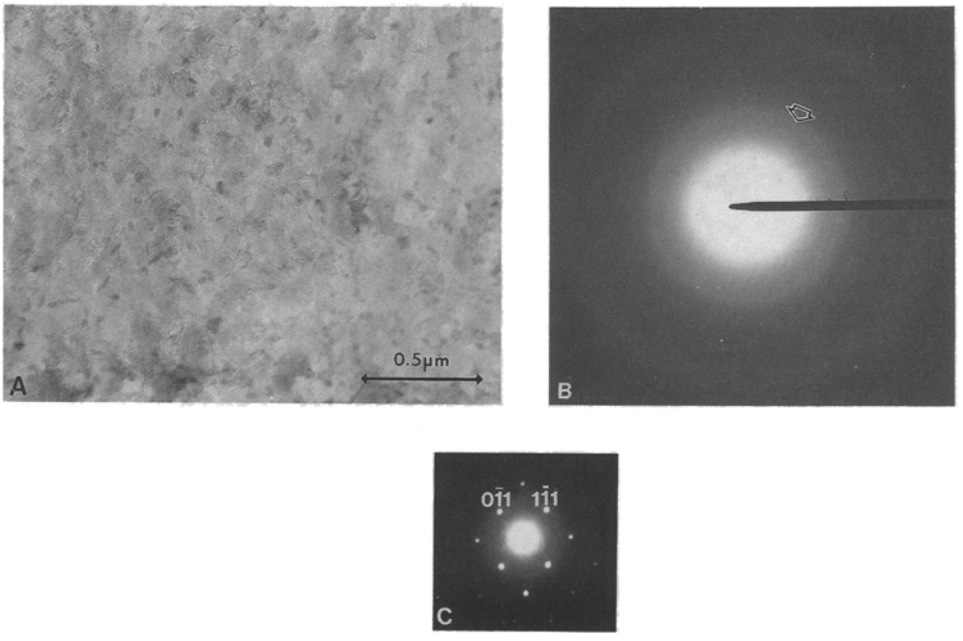

Fig. 9—Sample tempered at 482 °C: (*a*) bright-field image of the extraction replica showing small precipitates, (*b*) selected area diffraction showing a faint ring (arrow) corresponding to $\{1\bar{1}1\}_{M_2C}$, and (*c*) $[011]_{M_2C}$ pattern from an individual precipitate.

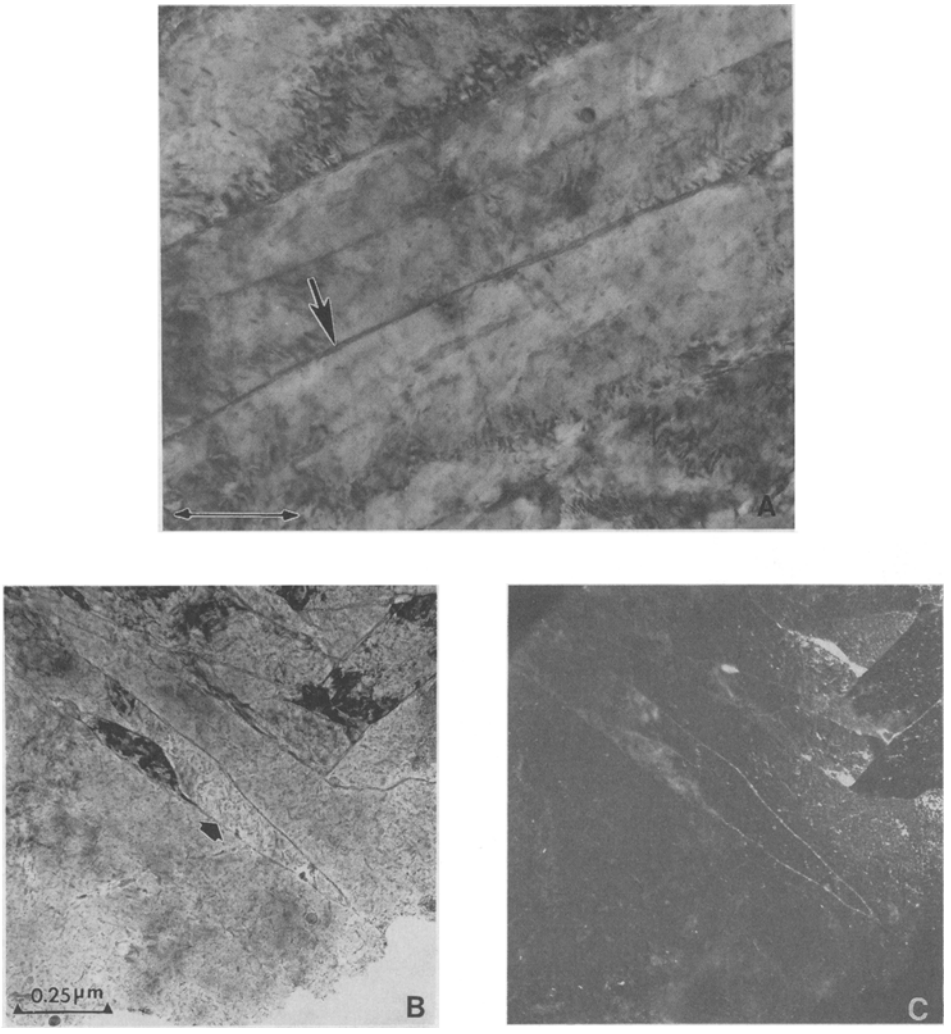

Fig. 10—Reverted austenite formation during tempering at 482 °C: (*a*) Bright-field image showing austenite (arrow), (*b*) defocussed bright-field image, and (*c*) corresponding dark-field image showing reversal of contrast of austenite.

slope of the curve increased. The corresponding change in the diameter of the precipitates was reasonably constant.

The metal content of the hexagonal M_2C carbide was determined in the carbon extraction replica for samples tempered from 482 °C to 566 °C. As observed in AF 1410 and related steels,[30] the carbides consisted essentially of Cr, Mo, and Fe. Figure 16 is a plot of the concentration of these elements in the carbides that formed at different tempering temperatures, the chromium content was found to decrease with increasing aging temperature with a corresponding increase in the molybdenum and iron contents. When the composition of the carbide is compared with the value reported for AF 1410, it is seen that the carbides in Aermet 100 have a higher iron content than that reported for AF 1410.

C. *Retained/Reverted Austenite*

Figure 17 shows the volume fraction of austenite determined by X-ray diffraction. The volume fraction in the as-quenched condition and subsequent to tempering at 427 °C indicated that the retained austenite in the steel was negligible, consistent with the TEM observations. Upon tempering at 454 °C and 482 °C, a small increase in the volume fraction of austenite was observed due to reversion; the volume fraction showed a rapid increase at and above 510 °C.

D. *RMS Strain*

The RMS strain was measured in order to follow the recovery process in the steel during tempering, since RMS studies have been successfully applied to follow the dislocation recovery in cold-rolled copper alloys. Figure 18 shows the plot of RMS strain along $[110]_\alpha$ for a 5-nm column length. The strain value was constant up to a tempering temperature of 510 °C, indicating that appreciable softening took place only above 510 °C. The small increase in the RMS value at 482 °C is considered to be within experimental scatter, and no significance was attached to it.

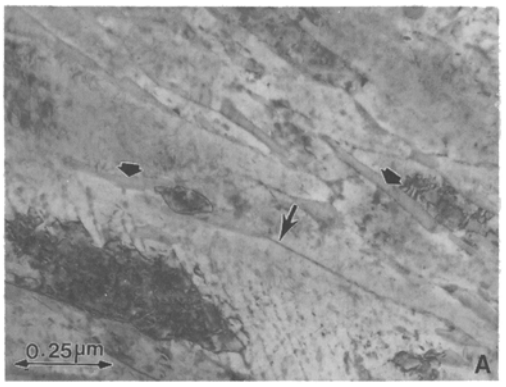

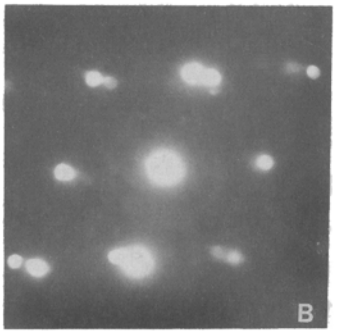

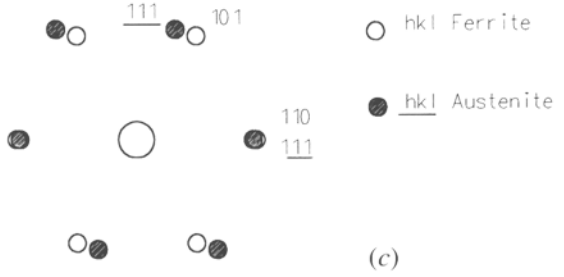

Fig. 11 — Sample tempered at 510 °C: (*a*) bright-field image showing reverted austenite (arrows), (*b*) electron diffraction pattern from the austenite shown in (*a*), and (*c*) Kurdjumov-Sachs orientation relationship between austenite and martensite.

IV. DISCUSSION

As indicated in Section I, the composition of Aermet 100 is similar to the popular AF 1410 steel with higher chromium and carbon content. Since extensive work has been performed in AF 1410,[18–30] the following discussion focuses on the similarities and differences between these two steels.

A. *Microstructural Evolution*

The results of the TEM examination on the as-quenched sample showed that the steel contained MC and $M_{23}C_6$ carbides. Similar carbides have been observed by other investigators in AF 1410 steel;[28] these carbides remained undissolved at the austenitization temperature and did not participate in the tempering reaction. As a result of a higher M_s temperature in AF 1410 steel (~580 °C), autotempering of the lath martensite occurred during cooling. These autotempered precipitates were identified as Widmanstätten cementite on the $\{110\}_\alpha$ planes.[16]

It was found that fine precipitates which formed upon tempering at 454 °C were coherent with the matrix. The primary evidence for coherency was the strain contrast in the bright-field images. In addition, the electron diffraction patterns also showed diffuse scattered intensity with no precipitate reflections. Irani and Honeycombe observed streaking at the early stage of tempering close to the peak hardness and attributed it to the formation of "zones" of unknown composition;[11] in a subsequent

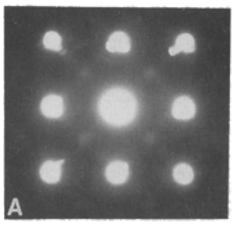

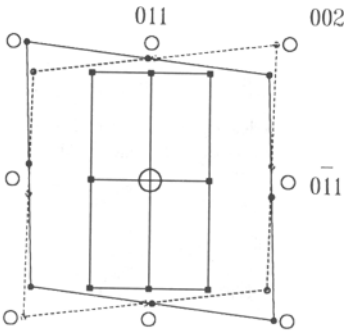

Fig. 12 — Sample tempered at 510 °C: (*a*) diffraction pattern from two variants of the precipitates in the plane of the thin foil and (*b*) schematic indexing of the pattern showing reflections expected from all three variants. Only reflections from the two variants in the plane of the foil (open and solid circles) are seen in Figure 13(a). The solid squares are the pattern from the end-on needles.

work, Raynor *et al.* attributed the streaking to M_2C precipitates.[5] However, they did not present convincing evidence for the presence of crystalline precipitates, as pointed out by Davies and Ralph.[10]

Based on the observations in the present study, it can be speculated that the precipitates after tempering at 454 °C were coherent zones of solute atoms. Many of the precipitates in the extraction replica of the 482 °C tempered sample did not yield diffraction spots, and the selected area pattern showed only a weak ring from the

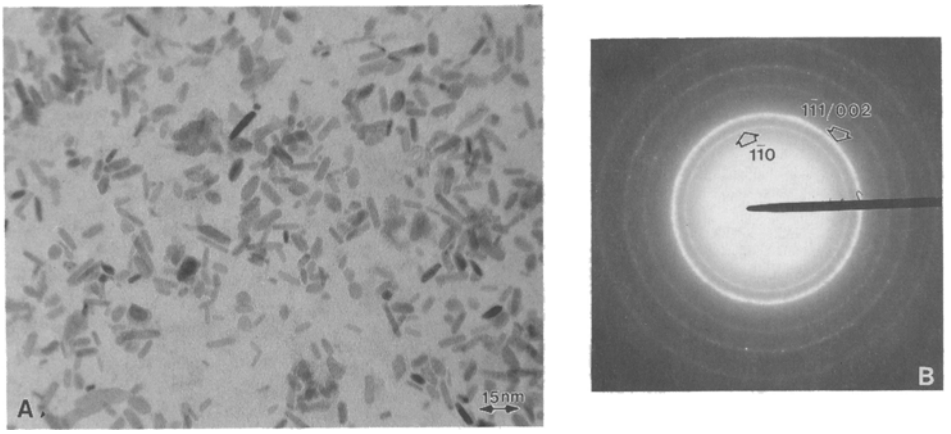

Fig. 13—Sample tempered at 510 °C: (*a*) bright-field image of the extraction replica showing high density of precipitates and (*b*) selected area diffraction pattern of (a) showing distinct rings from the hexagonal M_2C carbidesy. Two of the rings are indexed.

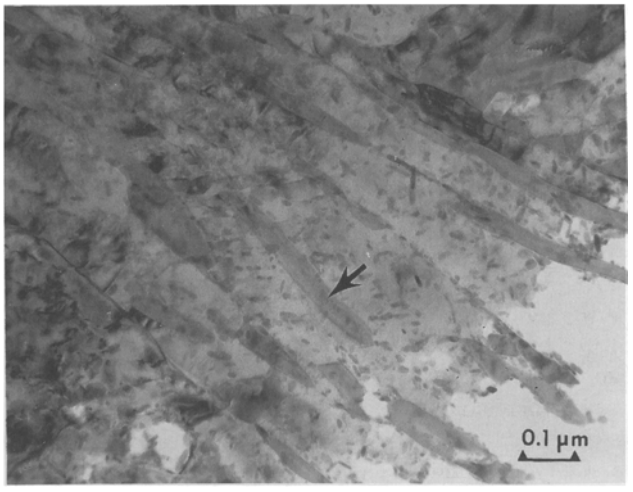

Fig. 14—Sample tempered at 538 °C; bright-field image of reverted austenite (arrow).

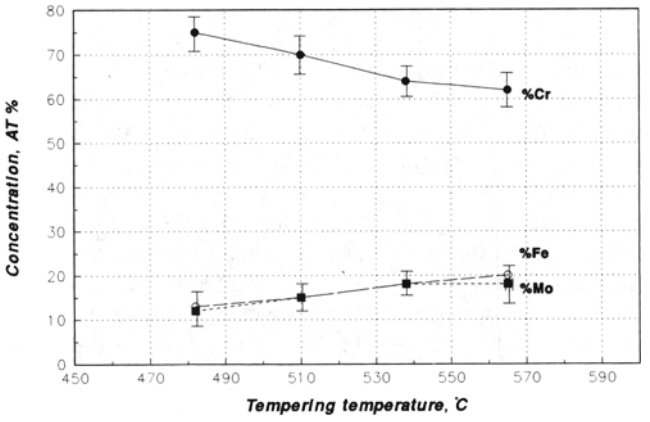

Fig. 16—Variation of the metallic elemental concentration in the M_2C carbides with tempering temperature.

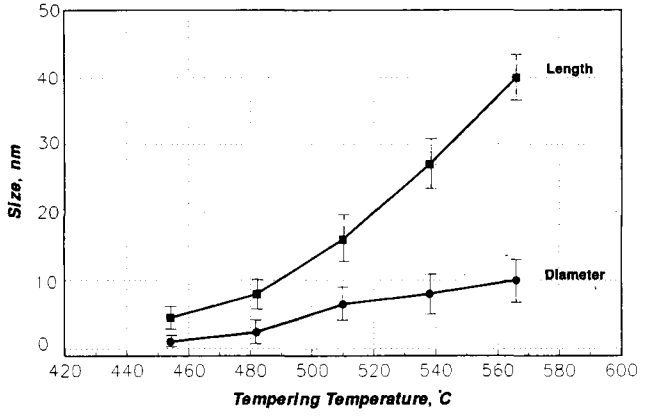

Fig. 15—Variation of the length and diameter of M_2C carbides with tempering temperature.

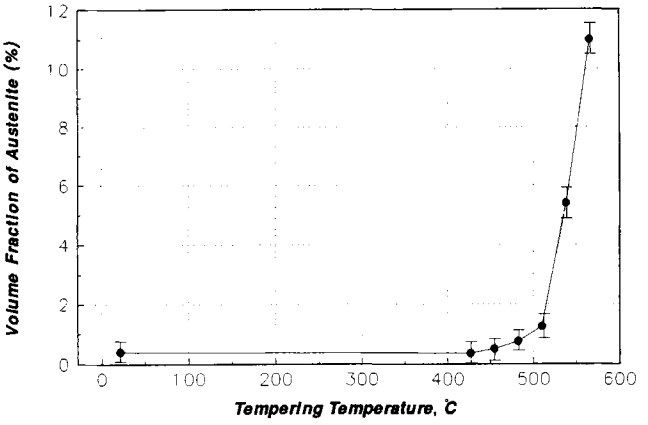

Fig. 17—Variation of volume fraction of retained or reverted austenite with tempering temperature.

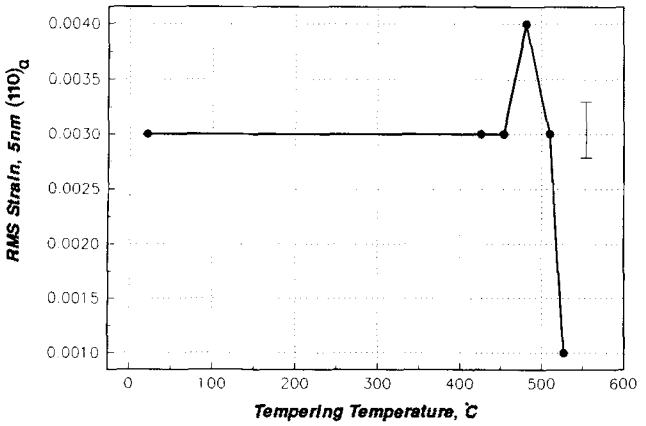

Fig. 18 — Variation of RMS strain of the martensite matrix with tempering temperature. Typical $\pm 3\sigma$ error bar is indicated.

hexagonal M_2C phase. This observation suggested that at least part of the precipitates in the 482 °C tempered condition were in the form of noncrystalline zones. Therefore, it can be argued that all the precipitates after 454 °C temper could be in the form of zones of solute clusters. Bright-field images of the end-on precipitates (Figure 6(a)) indicated that the zones were needle shaped. Recent APFIM studies on alloy AF 1410 by Olson *et al.* also indicated that at the early stages of tempering, the precipitates could be in the form of "clusters."[20]

An inflection point was observed in the plot of precipitate length and tempering temperature (Figure 15). The figure shows that at tempering temperatures above 482 °C, the precipitate length varied at a higher rate than at temperatures below 482 °C. Similar observations were reported by Montgomery and Olson in AF 1410 steel with 4 pct Mo[22] but not in AF 1410 steel. It is not clear if the inflection is associated with the loss of precipitate coherency or if it indicates the onset of particle growth. Additional work is required to establish the cause of the inflection.

In addition to precipitate coarsening, the other significant change upon tempering was the formation of reverted austenite. Austenite was found to form in a thin-film morphology at plate boundaries after tempering at 482 °C. Formation of reverted austenite within the plates was not observed at 482 °C or 510 °C. Since austenite was found essentially at the plate boundaries, it seems reasonable to propose that reversion occurred because tempering at 482 °C was at or above the A_{c_1} temperature for Aermet 100. Reversion was not due to enrichment of nickel around the M_2C carbides as proposed.[32] Therefore, it would appear that the A_{c_1} temperature for Aermet 100 is about 485 °C. The results of the TEM and X-ray diffraction studies showed that the formation of reverted austenite was first observed by TEM in the sample tempered at 482 °C, a corresponding X-ray diffraction analysis did not provide convincing support for the initiation of reversion. The detection of the initial formation of reverted austenite is extremely critical, since its thin-film morphology provides resistance to transformation during subsequent straining.

B. *Influence of Microstructure on Strength and Toughness*

The results of the present study have shown that the strength and toughness of the steel peaked at slightly different tempering temperatures. The yield and tensile strengths peaked at 468 °C, while the steel toughness peaked in the range of 482 °C to 510 °C (Figure 1). The peaks in the strength and toughness values corresponded to two distinct microstructural features.

The peak in strength at 468 °C was the result of a microstructure consisting of a uniform dispersion of extremely fine, needle-shaped coherent zones. Irani and Honeycombe suggested that molybdenum-rich zones formed on $\{100\}_\alpha$ planes, and subsequent diffraction studies revealed streaking along $\langle 100 \rangle$ directions.[9] These authors also observed that the streaking was present until peak aging. The present results also indicate that the peak strength is achieved when the precipitates are fully coherent with the matrix, in agreement with Irani and Honeycombe[9] and Olson.[20] Tempering at and above 510 °C resulted in total loss of precipitate coherency and a decrease in yield and tensile strengths. X-ray line broadening results also showed that the steel retained its as-quenched dislocation density up to a tempering temperature of 482 °C. This observation is consistent with the well-accepted concept that cobalt delays the recovery process during tempering.[14,16] Therefore, the strength in Aermet 100 steel is derived from (1) a high density of dislocations and (2) a fine dispersion of coherent precipitates.

An examination of the toughness variation during tempering indicated several important trends. The toughness of the as-quenched steel was high (160 MPa$\sqrt{\text{m}}$) which can be attributed to the low strength and the absence of coarse inclusions. The only precipitate particles in the as-quenched condition were the undissolved MC- and $M_{23}C_6$-type carbides. The cleanliness of the steel and relatively small and spherical-shaped carbides are the factors that provide superior toughness in the as-quenched condition.[20] However, potential exists for the improvement in steel toughness by refining the size of the $M_{23}C_6$ carbides, 20 to 100 nm in size, which were considerably larger than the MC carbides, 5 to 12 nm in size.

Upon tempering at 427 °C, the fracture toughness reached a minimum value. The microstructure at this tempering temperature consisted of coarse Widmanstätten cementite platelets at the plate and twin boundaries. It was initially pointed out by Speich for HY 180 steel[16] and by Machmeier for AF 1410 steel[18] that the presence of coarse particles would degrade the fracture toughness. Examination of the crack tip process zone in Aermet 100 steel (Figure 20) disclosed similar fracture behavior as previously observed in the AF 1410 steel.[18,29] The rapid drop in toughness after tempering at 427 °C can be attributed to a bifurcated type of mode II cracking where coarse carbides provided an easy crack path at the plate and prior austenitic grain boundaries. This fracture mode has been interpreted as a combination of transgranular (actual cleavage along {110} slip planes of martensite) and intergranular decohesion along plate

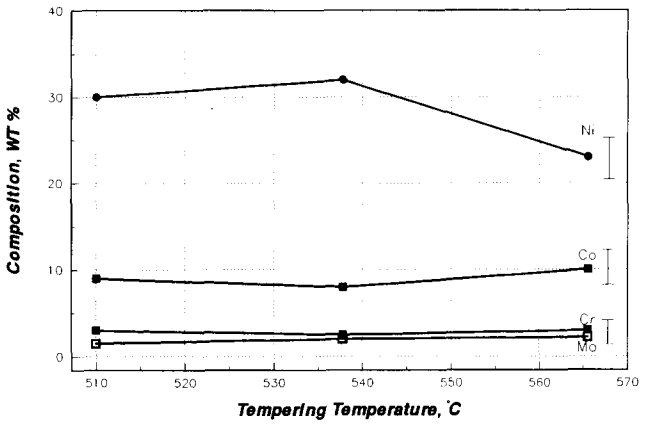

Fig. 19—Plot of metallic elemental concentration (weight percent) of reverted austenite.

boundaries. Tempering at the peak hardening temperature, 454 °C, resulted only in a modest increase (17 MPa$\sqrt{m}$) in toughness. Transmission electron microscopy observation showed that tempering at 454 °C resulted in the precipitation of sparse cementite particles only at the prior austenite grain boundaries. Therefore, the low toughness after tempering at this temperature can only be attributed to the undissolved cementite particles.

Tempering at 468 °C or 482 °C resulted in a sharp increase (~50 pct) in toughness. The microstructural features associated with this high toughness were (1) absence of cementite particles, (2) formation of thin-film reverted austenite at the plate boundaries, and (3) uniform precipitation of M_2C carbides.* Of these, factors (1) and (2) are proposed to be responsible for the enhanced toughness of the steel for the following reasons. In the as-quenched condition, the steel had a low yield strength (1300 MPa) and high toughness (160 MPa$\sqrt{m}$) which resulted from a uniform martensitic structure with finely dispersed $M_{23}C_6$ and MC carbides. Tempering at 468 °C or 482 °C resulted in toughness comparable to the as-quenched and cryogenically treated steel but at a considerably higher strength level. Thus, the strength/toughness ratio was higher in the sample tempered at 482 °C compared to the quenched and cryogenically treated sample. A comparison of the microstructures of these two conditions indicates that the primary difference that could account for the enhanced ratio is the presence of plate boundary austenite in the tempered sample. The reverted austenite had a thin-film morphology, similar to retained austenite observed in the as-quenched steels.[38] Thin-film morphology of reverted austenite has not been reported in similar steels; this can be attributed to the lower A_{c1} temperature of Aermet 100 compared to its predecessors, *viz.*, AF 1410 and HY 180. It is now well accepted that an enhancement in steel toughness can only be realized if the austenite is (1) present in a thin-film morphology and (2) resistant to transformation during externally imposed stress or strain.[20] These conditions are quite likely met when austenite reversion starts to occur, *viz.*, at 482 °C. At

*Although TEM examination was conducted only after tempering at 482 °C, it is assumed that the microstructures after 468 °C and 482 °C tempering were similar. The arguments presented would be valid even if only the 482 °C tempering results were considered.

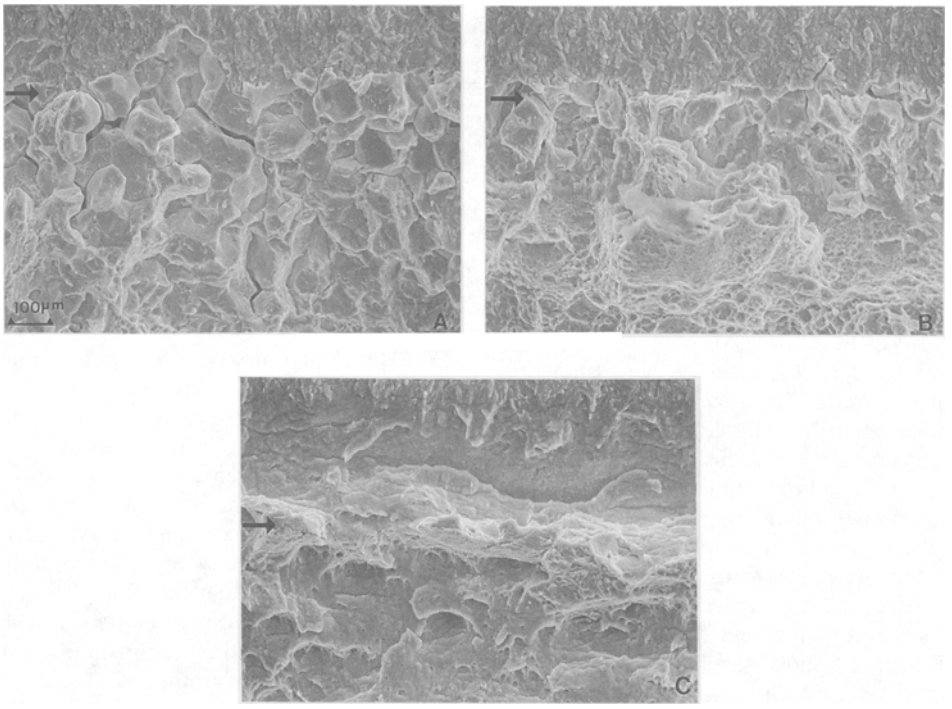

Fig. 20—Crack tip fracture behavior of fractured K_{Ic} sample as a function of tempering temperature: tempered at (*a*) 427 °C showing predominantly intergranular rupture and quasicleavage (K_{Ic} ~ 102.4 MPa$\sqrt{m}$); (*b*) 454 °C showing quasicleavage and void coalescence (K_{Ic} ~ 119.7 MPa$\sqrt{m}$); and (*c*) 482 °C high plastic strain shear (K_{Ic} ~ 149.3 MPa$\sqrt{m}$). The onset of fast fracture is indicated by arrows, and the direction of crack growth is from the top to the bottom of the images.

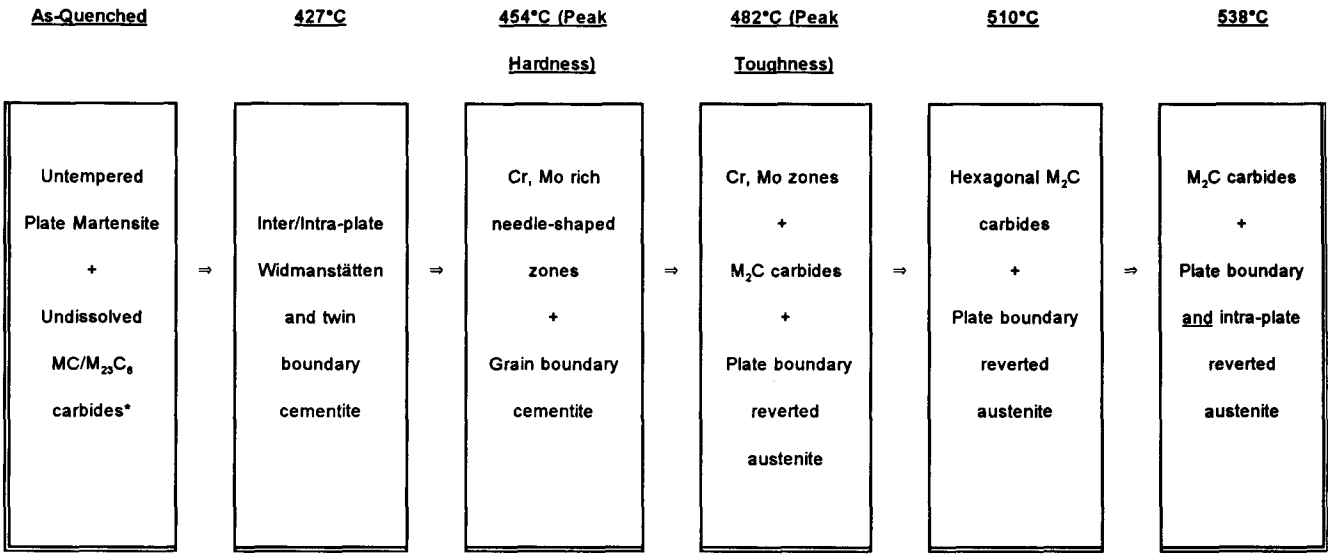

* carbides present at all tempering temperatures

this temperature, the solubility of nickel, cobalt, and carbon in austenite is relatively high. Austenite enriched in these solute elements would have a low M_d temperature and therefore would be resistant to transformation. Haidemenopoulos *et al.* demonstrated the beneficial contribution of reverted austenite in AF 1410 by double tempering.[23] These authors showed that additional toughening can be obtained by exposing the steel to higher temperatures to induce intraplate reverted austenite.

Tempering at 427 °C and higher temperatures also resulted in substantial changes in fracture behavior at the crack tip process zone, as shown in Figure 20. Under conditions of small scale yielding at the near crack tip field, the plastic zone fracture mechanism evolved from one with predominantly brittle inter- and transgranular fracture paths to one of high plastic shear strain accommodation concomitant with an approximately 50 pct increase in fracture toughness. Such an enhancement is possible in the absence of the coarse cementite particles and reverted austenite. A parallel increase in the axisymmetric tensile ductility properties (ε_f or percent reduction in area) by 23 and 12 pct, respectively, was also observed in the tempering range from 427 to 482 °C. This enhancement indicates that the critical plastic strain was not surpassed at the crack tip process zone, and therefore, ductile rupture occurred predominantly by the void nucleation and coalescence mechanism.

When the steel was tempered at temperatures in excess of 510 °C, coarse elongated regions of austenite formed. The austenite formed at these temperatures would have a relatively lower solute content and therefore a higher M_d temperature. Figure 19 shows a plot of the composition of the austenite (except carbon) in the tempering regime of 510 °C to 566 °C. The plot shows that when it was tempered at 510 °C and 538 °C, the composition of austenite did not change, but the nickel content showed a decrease when tempered at 566 °C. Similarly, the carbon content of the austenite is expected to decrease when tempered from 510 °C to 566 °C. Therefore, the reverted austenite at the higher tempering temperature would transform to martensite upon straining. Since the carbon content of this martensite is expected to be higher than the average carbon content of the steel, transformation during straining would impair the toughness, as observed in Figure 1. Over the range of tempering temperatures studied, the sequence of precipitation refers to the Schematic above.

V. SUMMARY

1. The maximum strength in Aermet 100 was achieved when the steel was tempered at 454 °C for 5 hours; the strengthening was attributed to the combination of delayed dislocation recovery of the martensitic matrix and the formation of needle-shaped, coherent precipitates along the ⟨100⟩ directions of the matrix. A drop in yield and tensile strengths upon overaging resulted from the loss of precipitate/matrix coherency.
2. The poor toughness observed upon tempering below the peak aging temperature (427 °C) was due the formation of coarse cementite particles at plate boundaries promoting brittle fracture.
3. The rapid increase (~50 pct) in toughness was observed when the steel was tempered at 482 °C; the increase was associated with the absence of coarse cementite particles and the formation of thin-film reverted austenite at the plate boundaries. Higher tempering temperatures resulted in a drop in toughness, probably caused by the instability of the reverted austenite during straining.

REFERENCES

1. K.H. Jack: *J. Iron Steel Inst.*, 1951, Nov., pp. 26-3611.
2. G.W. Greenwood: *Acta Metall.*, 1956, vol. 4, pp. 243-48.

3. K.J. Irvine: *J. Iron Steel Inst.*, 1962, Oct., pp. 820-33.
4. D. Raynor, J.S. Whiteman, and R.W.K. Honeycombe: *J. Iron Steel Inst.*, 1966, Nov., pp. 1114-16.
5. D. Raynor, J.A. Whiteman, and R.W.K. Honeycombe: *J. Iron Steel Inst.*, 1966, Apr., pp. 349-54.
6. D.J. Dyson, S.R. Keown, D. Raynor, and J.A. Whiteman: *Acta Metall.*, 1966, vol. 14, pp. 867-75.
7. T. Mukherjee, W.E. Stumpf, C.M. Sellars, and W.J. McG Tegart: *J. Iron Steel Inst.*, 1969, May, pp. 621-31.
8. S. Murphy and J.A. Whiteman: *Met. Sci. J.*, 1970, vol. 4, pp. 58-62.
9. A.T. Davenport and R.W.K. Honeycombe: *Met. Sci. J.*, 1975, vol. 9, pp. 201-08.
10. D.M. Davies and B. Ralph: *J. Iron Steel Inst.*, 1972, Apr., pp. 262-66.
11. J.J. Irani and R.W.K. Honeycombe: *J. Iron Steel Inst.*, 1965, Aug., pp. 826-33.
12. T. Tanino, T. Nishida, and K. Aoki: *J. Iron Steel Inst.*, 1967, Aug., pp. 874-75.
13. R.A. Clark and G. Thomas: *Metall. Trans. A*, 1975, vol. 6A, pp. 969-79.
14. V.K. Chandhok, J.P. Hirth, and E.J. Dulis: *Trans. ASM*, 1963, vol. 56, pp. 677-93.
15. V.K. Chandhok, J.P. Hirth, and E.J. Dulis: *Trans. AIME*, 1962, vol. 224, pp. 858-64.
16. G.R. Speich, D.S. Dabkowski, and L.F. Porter: *Metall. Trans.*, 1973, vol. 4, pp. 303-15.
17. G.R. Speich: in *Innovations in Ultrahigh Strength Steel Technology*, Proc. 34th Sagamore Army Materials Research Conf., G.B. Olson, M. Azrin, and E.S. Wright, eds., U.S. Army Materials Technology Laboratory, Watertown, MA, 1990, pp. 89-111.
18. P.M. Machmeier, C.D. Little, M.H. Horowitz, and R.P. Oates: *Met. Technol.*, 1979, pp. 291-96.
19. C.D. Little and P.M. Machmeier: U.S. Patent 4,076,525, 1978.
20. G.B. Olson: in *Innovations in Ultrahigh Strength Steel Technology*, Proc. 34th Sagamore Army Materials Research Conf., G.B. Olson, M. Azrin, and E.S. Wright, eds., U.S. Army Materials Technology Laboratory, Watertown, MA, 1990, pp. 3-66.
21. G.M. Carinci, G.B. Olson, J.A. Liddle, L. Chang, and G.D.W. Smith: in *Innovations in Ultrahigh Strength Steel Technology*, Proc. 34th Sagamore Army Materials Research Conf., G.B. Olson, M. Azrin, and E.S. Wright, eds., U.S. Army Materials Technology Laboratory, Watertown, MA, 1990, pp. 179-208.
22. J.S. Montgomery and G.B. Olson: in *Innovations in Ultrahigh Strength Steel Technology*, Proc. 34th Sagamore Army Materials Research Conf., G.B. Olson, M. Azrin, and E.S. Wright, eds., U.S. Army Materials Technology Laboratory, Watertown, MA, 1990, pp. 147-78.
23. G. Haidemenopoulos, G.B. Olson, and M. Cohen: in *Innovations in Ultrahigh Strength Steel Technology*, Proc. 34th Sagamore Army Materials Research Conf., G.B. Olson, M. Azrin, and E.S. Wright, eds., U.S. Army Materials Technology Laboratory, Watertown, MA, 1990, pp. 549-93.
24. M. Schmidt and M. Gore: in *Innovations in Ultrahigh Strength Steel Technology*, Proc. 34th Sagamore Army Materials Research Conf., G.B. Olson, M. Azrin, and E.S. Wright, eds., U.S. Army Materials Technology Laboratory, Watertown, MA, 1990, pp. 407-24.
25. J.A. Liddle, G.D.W. Smith, and G.B. Olson: *Proc. 33rd Int. Field Emission Symp.*, appeared in *J. Phys.*, 1986, vol. 47, pp. C7-223-C7-31.
26. G.B. Olson, T.J. Kinkus, and J.S. Montgomery: *Surf. Sci.*, 1991, vol. 246, pp. 238-45.
27. G. Haidemenopoulos, M. Grujicic, G.B. Olson, and M. Cohen: *Acta Metall.*, 1989, vol. 37, pp. 207-18.
28. M.J. Gore, G.B. Olson, and M. Cohen: *Acta Metall.*, 1989, vol. 37, pp. 425-41.
29. K.J. Handerhan, W.M. Garrison, Jr., and N.R. Moody: *Metall. Trans. A*, 1989, vol. 20A, pp. 105-23.
30. H.M. Lee, A.J. Garratt-Reed, and S.M. Allen: *Scripta Metall. Mater.*, 1991, vol. 25, pp. 685-88.
31. M. Schmidt and R. Hemphill: *Scripta Metall. Mater.*, 1991, vol. 25, pp. 239-60.
32. P.M. Novotny: in *Fundamentals of Aging and Tempering in Bainite and Martensitic Steel Products*, Gilbert Speich Symp. Proc., Iron and Steel Society, Warrendale, PA, 1992, pp. 215-36.
33. Raghavan Ayer and P. Machmeier: in *Microstructure and Mechanical Properties of Aging Materials*, Int. Symp., ASM, Metals Park, OH, 1992.
34. R.L. Miller: *Trans. ASM*, 1964, vol. 57, pp. 892-99.
35. B.E. Warren: *J. Appl. Phys.*, 1941, vol. 12, pp. 375-89.
36. B.E. Warren and B.L. Averbach: *J. Appl. Phys.*, 1950, vol. 21, pp. 21-34.
37. P. Ganesan, H.K. Kuo, A. Saavedra, and R.J. DeAngelis: *J. Catalysis*, 1978, vol. 52, pp. 310-20.
38. G. Thomas: *Metall. Trans. A*, 1978, vol. 9A, pp. 439-50.
39. H. Smith and D.R.F. West: *J. Mater. Sci.*, 1973, vol. 8, pp. 1413-20.